REPORT DOCUMENTATION PAGE

1. REPORT DATE (DD-MM-YYYY)	2. REPORT TYPE	3. DATES COVERED (From - To)
30-07-2008	REPRINT	

4. TITLE AND SUBTITLE

Large-angle xenon ion scattering in Xe-propelled electrostatic thrusters: differential cross sections

5a. CONTRACT NUMBER

5b. GRANT NUMBER

5c. PROGRAM ELEMENT NUMBER
61102F

6. AUTHORS

Y-H. Chiu
R.A. Dressler
D.J. Levandier*
C. Houchins**
C.Y. Ng**

5d. PROJECT NUMBER
2303

5e. TASK NUMBER
RS

5f. WORK UNIT NUMBER
A1

7. PERFORMING ORGANIZATION NAME(S) AND ADDRESS(ES)

Air Force Research Laboratory /RVBXR
29 Randolph Road
Hanscom AFB, MA 01731-3010

8. PERFORMING ORGANIZATION REPORT NUMBER

AFRL-RV-HA-TR-2008-1056

9. SPONSORING/MONITORING AGENCY NAME(S) AND ADDRESS(ES)

10. SPONSOR/MONITOR'S ACRONYM(S)
AFRL/RVBXR

11. SPONSOR/MONITOR'S REPORT NUMBER(S)

12. DISTRIBUTION/AVAILABILITY STATEMENT
Approved for Public Release; distribution unlimited.

20080819 340

14. ABSTRACT Elastic scattering between xenon ions and xenon atoms can produce ion currents at large angles with respect to the axis of electrostatic thrusters. Differential scattering cross sections are needed to properly predict off-axis currents that can cause significant material erosion due to sputtering. Guided-ion beam differential cross section measurements are presented for $Xe^+ + Xe$ and $Xe^{2+} + Xe$ elastic scattering at laboratory ion energies between 5 and 40 eV per ion charge. For the singly charged system, the experimental absolute differential cross sections are in excellent agreement with classical elastic scattering calculations based on the most recent *ab initio* ion-atom interaction potentials. The measurements for the doubly charged system are used to derive an approximate effective Xe^{2+} - Xe interaction potential. The potentials are used to calculate absolute differential cross sections for both ion charge states at a typical Hall thruster ion of 270 eV per unit charge. The differential cross sections for the doubly charged ions are approximately a factor of 3 smaller than those of the singly charged system at large scattering angles. The importance of doubly charged ions with respect to material erosion is discussed on the basis of known sputtering yields as a function of ion energy for molybdenum and boron nitride. It is concluded that at typical charge-state ratios, doubly charged ions only have an impact at scattering angles where the scattered ion energy in the laboratory (thruster) frame of reference is low and the sputtering yields depend very strongly on ion energy.

15. SUBJECT TERMS

Xenon ion collision   Emission excitation cross section   Ion beam luminescence spectra   Electric thruster
Hall effect thruster

16. SECURITY CLASSIFICATION OF:			17. LIMITATION OF ABSTRACT	18. NUMBER OF PAGES	19a. NAME OF RESPONSIBLE PERSON
a. REPORT	b. ABSTRACT	c. THIS PAGE			Y-H. Chiu
UNCL	UNCL	UNCL	UNL	11	19B. TELEPHONE NUMBER (Include area code)

Standard Form 298 (Rev. 8/98)
Prescribed by ANSI Std. Z39.18

DTIC COPY

Large-angle xenon ion scattering in Xe-propelled electrostatic thrusters: differential cross sections

Y-H Chiu[1], **R A Dressler**[1,4], **D J Levandier**[2], **C Houchins**[3] **and C Y Ng**[3]

[1] Air Force Research Laboratory, Space Vehicles Directorate, Hanscom AFB, MA 01731, USA
[2] Institute for Scientific Research, Boston College, Chestnut Hill, MA 02159, USA
[3] Department of Chemistry, University of California, Davis, CA 95616, USA

E-mail: AFRL.RVB.PA@hanscom.af.mil

Abstract

Elastic scattering between xenon ions and xenon atoms can produce ion currents at large angles with respect to the axis of electrostatic thrusters. Differential scattering cross sections are needed to properly predict off-axis currents that can cause significant material erosion due to sputtering. Guided-ion beam differential cross section measurements are presented for $Xe^+ + Xe$ and $Xe^{2+} + Xe$ elastic scattering at laboratory ion energies between 5 and 40 eV per ion charge. For the singly charged system, the experimental absolute differential cross sections are in excellent agreement with classical elastic scattering calculations based on the most recent *ab initio* ion–atom interaction potentials. The measurements for the doubly charged system are used to derive an approximate effective Xe^{2+}–Xe interaction potential. The potentials are used to calculate absolute differential cross sections for both ion charge states at a typical Hall thruster ion energy of 270 eV per unit charge. The differential cross sections for the doubly charged ions are approximately a factor of 3 smaller than those of the singly charged system at large scattering angles. The importance of doubly charged ions with respect to material erosion is discussed on the basis of known sputtering yields as a function of ion energy for molybdenum and boron nitride. It is concluded that at typical charge-state ratios, doubly charged ions only have an impact at elastic scattering angles where the scattered ion energy in the laboratory (thruster) frame of reference is low and the sputtering yields depend very strongly on ion kinetic energy.

1. Introduction

In electrostatic thrusters [1, 2], such as Hall effect thrusters (HETs) [3, 4] and ion thrusters [5, 6], a gaseous propellant, preferably Xe, is efficiently ionized in a discharge and ions are accelerated to high energies by acceleration voltages between 0.2 and 2 kV. The accelerated ions are scattered in collisions with residual neutrals. Large-angle scattered ions contribute to a number of problems, including insulator erosion in the discharge channel of Hall thrusters, grid erosion in ion thrusters and sputtering of sensitive surfaces of the host spacecraft [7–9]. Proper integration of electrostatic thrusters requires accurate modelling of the expanding plasma and associated

ion currents to minimize detrimental effects due to ion–surface impingement. Critical parameters for correct quantification of these currents are ion differential scattering cross sections.

In the case of Xe-propelled electrostatic thrusters, angular scattering cross sections, i.e. differential cross sections, have been calculated for the $Xe^+ + Xe$ collision system using available *ab initio* potentials and neglecting effects due to inelastic scattering [7–9]. Approximately 10% of xenon ions in an electrostatic thruster plasma are doubly charged [10]. If differential scattering cross sections for Xe^{2+} are comparable to those of the singly charged ion, doubly charged ions may play a significant role in surface erosion since they are associated with higher sputtering yields due to kinetic energies that are twice those of Xe^+ ions. No potentials are available for the more complicated $Xe^{2+} + Xe$ collision system, and thus no

---

[4] Current address: Spectral Sciences, Inc., 4 Fourth Avenue, Burlington, MA 01803, USA.

elastic differential cross sections have been calculated to date.

The measurement of absolute ion scattering differential cross sections presents significant experimental challenges. To date, experimental scattering experiments of rare gas ions in their parent gases have consisted of crossed beam experiments that concentrated on small scattering angles, where structure due to quantum interferences is observed [11]. Crossed beam experiments have high energy and angular resolution but lose sensitivity at large angles and more importantly, they do not yield absolute cross sections due to the difficulty in determining absolute target gas densities.

In this paper, we report measurements of absolute differential cross sections for large-angle scattering of Xe^+ and Xe^{2+} by Xe atoms using the guided-ion beam time-of-flight (GIB–TOF) technique developed by Teloy and Gerlich [12, 13]. In this experiment, the scattering occurs within a cylindrical ion trap or ion guide, where the trap axis coincides with the beam axis, and all scattered ions are collected provided the guiding field is sufficient to collect ions with the highest velocity components perpendicular to the trap axis. Time-resolved measurements result in absolute differential cross sections with full collection efficiency at large scattering angles [14, 15], thereby overcoming many drawbacks of crossed beam experiments. The GIB–TOF methodology pays a significant penalty in angular resolution, particularly at low scattering angles. This weakness is mitigated by deriving differential cross sections from the experimental data using a deconvolution approach based on determining the effective scattering potential that reproduces the observed measurements at multiple collision energies.

Our approach is first validated by comparing the experimental scattering distributions at selected collision energies obtained for the $Xe^+ + Xe$ system with calculated distributions based on elastic differential cross sections determined from the most recent spin–orbit free *ab initio* interaction potentials by Paidarova and Gadea [16]. An effective potential is then derived from corresponding scattering distributions observed for the $Xe^{2+} + Xe$ system at several energies. Ultimately, differential cross sections for the doubly charged system are calculated from the derived potential for a typical Hall thruster acceleration potential of 300 V.

This paper is organized as follows: the experimental approach is described briefly in section 2. The theory behind the analysis of the present experiments is described in section 3, with particular emphasis on the complication due to symmetric charge exchange (SCX). Results for scattering of singly and doubly charged ions are presented and discussed in section 4.

2. Experiment

The apparatus used for the cross section measurements is a modified version of an instrument described in detail previously [17,18]. Xenon ion beams are produced by electron impact ionization of an effusive Xe gas source (99.999%, Spectra Gases). Nominal electron energies of 18 and 40 eV are applied for the formation of Xe^+ and Xe^{2+}, respectively. The Xe^+/Xe^{2+} primary ion beam has a ~0.2 eV per charge
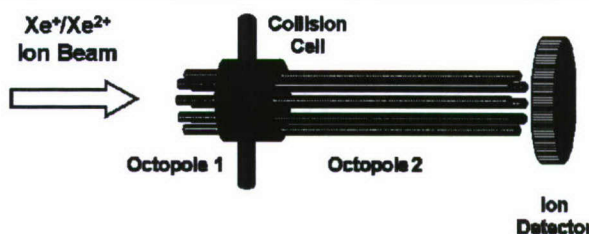

Figure 1. Schematic representation of the ion–atom collision and detection region of the guided-ion beam (GIB) scattering experiment.

full width at half maximum energy spread and is accelerated into a Wien velocity filter for mass/charge selection, and then injected into an ion guide system consisting of two rf octopoles in tandem. Figure 1 shows the schematic of the ion guide configuration used. The first octopole guides the ion beam through a cell which contains a target gas at low pressure (~0.2 mTorr) to ensure single collision conditions. The second longer octopole is 19.63 cm long and guides both the primary and the scattered ions through a low pressure region for the time-of-flight (TOF) analysis. We have replaced the extraction ion optics and quadrupole mass filter used in traditional GIB experiments [12, 19] with an on-axis, large aperture electron multiplier at the exit of the guide. This experiment does not require a mass filter since primary and scattered ions, apart from a minor channel due to asymmetric charge-transfer products in $Xe^{2+}+Xe$ collisions, have the same mass-to-charge ratio. Coupling of a mass filter to the second octopole leads to losses of ions with large transverse velocity components [20] in the extraction optics. This configuration without mass filter ensures that all scattered ions, in particular large-angle scattered ions with large transverse components, are efficiently collected and detected.

The experiment is operated in a pulsed TOF mode, and the primary and scattered ions are distinguished by their separate arrival times. The second octopole is biased ~0.4 V below the first octopole to permit ions with very low laboratory velocities to reach the detector. ~100 V is applied to a cylindrical ring electrode surrounding the octopole at the entrance of the collision cell. This produces a small potential barrier of ~100 mV within the octopole that reflects laboratory backscattered ions into the forward direction. To avoid background signals due to ions trapped for multiple repetition periods, the rf voltage on the octopole is briefly switched off prior to each TOF period to purge slow residual ions formed by previous ion pulses.

The acquired arrival time spectra are inverted to laboratory velocity distributions, $I(v_p)$, where v_p is the ion velocity component parallel to the beam and octopole axis. An rf frequency of ~8.16 MHz is used and rf amplitudes are applied to achieve effective potentials that ensure collection of ions scattered at 90° in the centre-of-mass (CM) frame, where the highest transverse velocities are expected.

Under single collision conditions, the absolute differential cross section in the GIB–TOF frame of reference can be
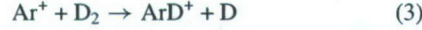
expressed as

$$\frac{d\sigma(v_p)}{dv_p} = \frac{I(v_p)\Delta v_p}{I_0 nl}, \tag{1}$$

where Δv_p is the velocity bin width and I_0 is the primary ion Xe^+/Xe^{2+} intensity,

$$I_0 = \int_0^\infty I(v_p)\,dv_p, \tag{2}$$

n is the number density of the neutral Xe target and l is the effective length of the primary ion–neutral interaction region. The latter is calibrated using the well-known reaction [21]

$$Ar^+ + D_2 \rightarrow ArD^+ + D \tag{3}$$

that is characterized by strong forward scattering of reaction products and is thus minimally affected by discrimination in the collection optics. The calibration measurements were carried out in the conventional experimental setup including extraction optics and a quadrupole mass filter prior to ion detection [17]. The uncertainty of the cross sections is estimated to be ±30%. The cross sections are corrected with respect to background gas contributions by subtracting cross sections obtained when the target gas is diverted directly into the vacuum chamber without passage through the cell.

This experiment needs to ensure that the rf amplitude applied to the octopole is sufficient to confine the maximum transverse velocity component, v_t, of scattered ions. The effective confinement field generated by the rf voltage on the octopole rods is calibrated using a previously reported approach [13]. The resolution with respect to the transverse translational energy component is ~0.2 eV.

3. Analysis

3.1. Absolute elastic scattering differential cross sections of SCX systems

SCX is an elastic process (no translational energy transfer). Due to high SCX cross sections, it is crucial to include SCX effects in the $Xe^+ + Xe$ and $Xe^{2+} + Xe$ elastic scattering angular distributions. Elastic scattering of SCX systems is best understood by examining the Newton scattering diagram in figure 2. In symmetric ion–atom systems, the CM velocity is half the laboratory ion velocity, $v(Xe^+/Xe^{2+})$. The diagram indicates two scattering possibilities, one producing maximum transverse velocities at a CM scattering angle, $\Theta_{CM} = 90°$, and one at $\Theta_{CM} \approx 30°$. The corresponding laboratory (lab) scattering angle, $\Theta_{LAB} = \frac{1}{2}\Theta_{CM}$, is also indicated for the acute angle. The scattered velocity vectors are referred to as primed u and v vectors in the CM and lab frames, respectively.

At acute angles, SCX causes the ion to be backscattered in the CM frame, and the ion scattering angle becomes $\pi - \Theta_{CM}$. At $\Theta_{CM} = 90°$, the absolute scattering angles of the ion and atom are the same. In the present singly and doubly charged SCX systems, the SCX probabilities, $P_{SCX}(b)$, are such that they become oscillatory, varying between 0 and 1 below collision impact parameters, b, corresponding to scattering angles of the order of 1° at the collision energies of interest (see
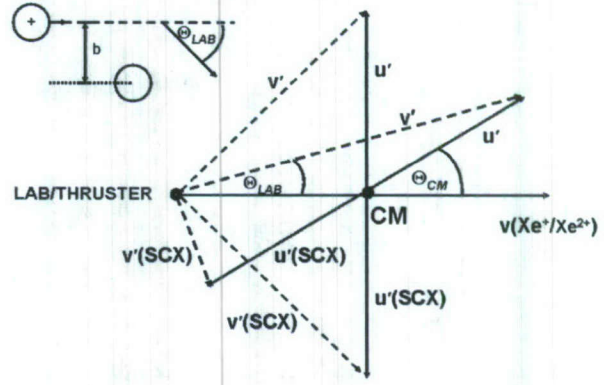

Figure 2. Newton diagram for elastic scattering in symmetric ion–atom collisions. v is the laboratory ion velocity, v' is the laboratory scattered ion velocity, $v'(SCX)$ is the laboratory scattered ion velocity of charge exchange ions and u' and $u'(SCX)$ are the corresponding scattered CM velocities. The inserted diagram at the top left defines the impact parameter, b, and laboratory scattering angle of an ion–atom collision.

figure 2). Consequently, at significant scattering angles, the SCX probability averages to a value of 0.5 at the experimental resolution. Large-angle scattered ions thus have significant contributions from both direct and SCX ions.

The differential cross sections, $d\sigma(\theta_{CM})/d\Omega_{CM}$, where $\theta = |\Theta_{CM}|$, $0 < \theta < \pi$, and $d\Omega_{CM} = 2\pi \sin\theta_{CM}d\theta_{CM}$, can, therefore, be calculated in two steps: calculation of elastic scattering differential cross sections from the deflection function, $\Theta_{CM}(b)$, followed by the calculation of $P_{SCX}(b)$ and the associated angular transformation to derive ion-specific differential cross sections that incorporate charge exchange. This process has been discussed in previous work [7], and will be summarized briefly with particular attention to the second step that has to be conducted at a higher level of precision to properly scale calculated TOF velocity distributions based on the determined differential cross sections. The deflection angle caused by an ion–atom interaction potential, $V_i(R)$, at a CM collision energy, E_T, is determined from [22]

$$\Theta_{CM_i}(E_T, b) = \pi - 2b \int_{R_0}^\infty \frac{dR}{R^2[1 - b^2/R^2 - V_i(R)/E_T]^{1/2}}, \tag{4}$$

where R is the interatomic distance and R_0 is the turning point or closest point of approach of the trajectory. The differential cross section associated with potential $V_i(R)$ at an energy of E_T is then obtained from

$$\frac{d\sigma_i(\theta_{CM_i}, E_T)}{d\Omega_{CM}} = \sum_j \left| \frac{b_j}{\sin(\theta_{CM_i})d\theta_{CM_i}/db} \right|, \tag{5}$$

where b_j are the impact parameters associated with the corresponding scattering angle. Except for scattering angles associated with turning points in the vicinity of potential wells where there are three b_j values, there is only one b_j value to consider for each scattering angle. The total differential cross section is then obtained from

$$\frac{d\sigma(\theta_{CM}, E_T)}{d\Omega_{CM}} = \sum_i d_i \frac{d\sigma_i(\theta_{CM_i}, E_T)}{d\Omega_{CM}}, \tag{6}$$
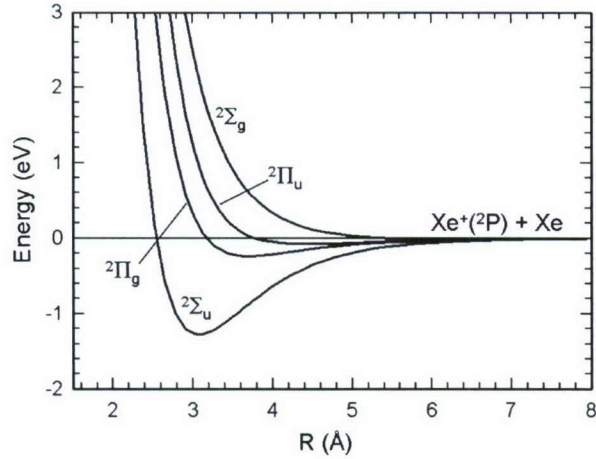
Figure 3. Spin–orbit free interaction potentials, calculated by Paidarova and Gadea [16], between the ground states of Xe$^+$ and Xe.

where d_i are the statistical weights of the potential, $V_i(R)$, accessed by the colliding atom and ion. For Xe$^+$+Xe collisions, the four spin–orbit free potentials, $^2\Sigma_u$, $^2\Sigma_g$, $^2\Pi_u$ and $^2\Pi_g$, calculated by Paidarova and Gadea [16], are considered. These potentials with statistical weights 1/6, 1/6, 1/3 and 1/3, respectively, are shown in figure 3. We have verified that using the full spin–orbit potentials derived from these potentials assuming that the spin–orbit coupling constant is independent of the interatomic distance, R, does not significantly change the scattering results when a statistical population of the two lowest $^2P_{3/2}$ and $^2P_{1/2}$ atomic spin–orbit states of Xe$^+$ is assumed. Since the electronic coupling between the *gerade* (g) and the *ungerade* (u) states of the same symmetry causes rapid hopping between them, the differential cross sections are calculated using Morse potential fits to the averaged u, g pairs. The potentials for Xe^{2+}+Xe have not yet been calculated using *ab initio* quantum chemical methods. For fitting to the experimental data, a combination potential, Morse-repulsive, is assumed:

$$V(R) = a_1(e^{a_2(a_3-R)^2} - 2e^{a_2(a_3-R)}) + (a_4 + a_5/R)e^{-a_6R}, \quad (7)$$

where a_1, a_2, a_3 are Morse potential function-like parameters, and a_4, a_5, a_6 are parameters representing a repulsive potential functional form.

The effect of charge exchange is added to derive the differential cross section specific to ions by conducting the following transformation:

$$\frac{d\sigma_{ion}(\theta_{CM})}{d\Omega_{CM}} = \{1 - P_{SCX}(\theta_{CM})\}\frac{d\sigma(\theta_{CM})}{d\Omega_{CM}}$$
$$+ P_{SCX}(\theta_{CM})\frac{d\sigma(\pi - \theta_{CM})}{d\Omega_{CM}}, \quad (8)$$

where $P_{SCX}(\theta_{CM})$ is the angle-dependent SCX probability. Through the deflection function, $P_{SCX}(\theta_{CM})$ is related to $P_{SCX}(b)$, which is given by [8,23]

$$P_{SCX}(b) = \sum_i d_i \sin^2(\eta_i^g - \eta_i^u), \quad (9)$$

where $\eta_i^{u,g}$ are the elastic scattering phase shifts for scattering by the respective potentials at the specified impact parameter. Standard methods can be applied for the calculation of $P_{SCX}(b)$. They are based on the electronic coupling or exchange energy, which is given by $\Delta V(R) = V_g(R) - V_u(R)$ [24]. Since the potentials for Xe$_2^{2+}$ are not known, an approximate approach is necessary to estimate the electronic coupling for the doubly charged collision system. We have determined [23] that an expression derived from polarization perturbation theory [25],

$$\Delta V(R) = \frac{8}{e}E_1R\exp(-\alpha_1 R), \quad (10)$$

reproduces experimental SCX cross sections for Xe^{2+} + Xe when the ionization energy, E_1, is chosen to be the energy to remove two electrons from a Xe atom. The coupling parameter in the exponent is given by $\alpha_1 = (2E_1)^{1/2}$. The integral charge exchange cross section, σ_{SCX}, is given by

$$\sigma_{SCX} = 2\pi \int_0^\infty P_{SCX}(b)b\,db. \quad (11)$$

3.2. Deriving the effective Xe^{2+} + Xe interaction potential

The objective of this work is to derive an effective potential from the differential scattering experiments by fitting parameters of functional form (7) to reproduce the experimental data at several collision energies. Simulated TOF spectra, $I(v_p)$, are obtained by calculating the kinematically broadened distributions by convoluting the differential cross sections with the appropriate Jacobians using a previously reported approach [19, 26]. While the experimental distributions are put on an absolute scale through equation (1), the simulations are normalized with respect to the SCX cross section as obtained from the angle integration of the differential cross sections used for the simulation. Since most of the SCX scattering occurs at ion scattering angles near π, the SCX cross section can be approximated by (see figure 2):

$$\sigma_{SCX}^{sim} = 2\pi \int_{\pi/2}^\pi \left(\frac{d\sigma_{ion}(\theta_{CM})}{d\Omega_{CM}}\right)\sin\theta_{CM}\,d\theta_{CM}. \quad (12)$$

This cross section should be equal to that obtained from equations (9)–(11). Since SCX scattering is dominated by scattering near the singularity $\theta_{CM} = \pi$, minor differences can arise between the angle and impact parameter integrated approaches due to integration inaccuracies. Using equation (12) ensures that the simulation is scaled properly with respect to the absolute differential cross sections and not the expected, more accurate SCX cross section obtained with equation (11). The simulations are then converted to absolute differential cross sections using the expression

$$\frac{d\sigma^{sim}(v_p)}{dv_p} = \frac{I^{sim}(v_p)\sigma_{SCX}^{sim}}{\int_0^{v_{CM}} I^{sim}(v_p)\,dv_p}. \quad (13)$$

The integration in the denominator provides the approximate SCX signal, where the signal at $v_p = 0$ and v_{CM}, the CM velocity of the collision system, corresponds to scattering at
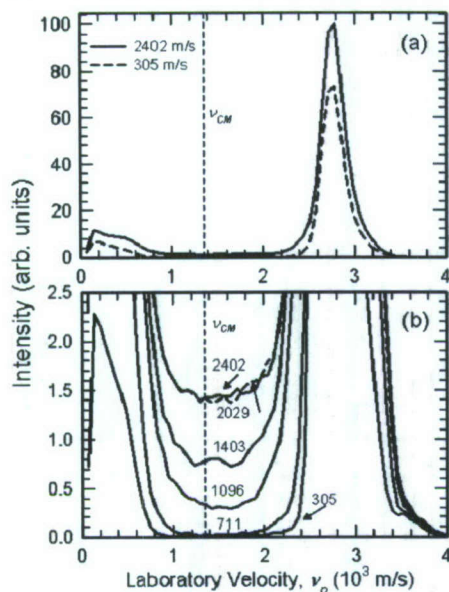
J. Phys. D: Appl. Phys. **41** (2008) 165503

Y-H Chiu *et al*

Figure 4. (*a*) Velocity inverted TOF distributions of Xe$^+$ + Xe collisions at an ion energy of 5 eV. The two distributions were recorded at two rf amplitudes corresponding to confinement fields with maximum transmitted transverse velocities of 2402 and 305 m s^{-1}. (*b*) Vertically expanded view of TOF distributions at several rf amplitudes with corresponding indicated maximum transmitted transverse velocities. The vertical dashed line in both charts corresponds to the CM velocity.

Figure 5. Velocity inverted TOF distributions (solid circles) for Xe$^+$ + Xe collisions at laboratory ion energies per charge of 5, 10, 15 and 20 eV. The solid lines are calculated distributions based on elastic scattering by the potentials reported by Paidarova and Gadea [16].

$\theta_{CM} = \pi$ and $\pi/2$, respectively, provided inelastic scattering is negligible. The comparison with measurements requires scaling of the 'unscattered' ($\theta_{CM} = 0$) ion intensity. This is accomplished by adjusting the differential cross section at the lowest specified angle so that the 'unscattered' intensity compares with that of the experiment. The angle grid is chosen such that $P_{SCX} = 0$ for the smallest angles.

The differential cross sections for Xe^{2+} + Xe collisions are obtained by adjusting the potential parameters of equation (7) to provide the best fit of the experimental TOF distributions at all investigated ion energies, in particular the signal in the vicinity of v_{CM}.

4. Results and discussion

4.1. Differential cross sections

Figure 4(*a*) shows velocity inverted TOF measurements, $I(v_p)$, for Xe$^+$ + Xe collisions at a laboratory ion energy of 5 eV. Two measurements are shown that were recorded at a high and a low confinement field corresponding to a maximum transmitted transverse velocity, v_t, of 2402 m s^{-1} (solid) and 305 m s^{-1} (dashed), respectively. The two distributions are put on the same absolute vertical scale by ensuring that the total integrated intensity corresponds to the transmitted ion current at the corresponding rf amplitude. The vertical dashed lines indicate the CM velocity, v_{CM}, of the collision system. The axial velocities of the primary ions peak at ∼2710 m s^{-1} and the second peak at near-thermal velocities

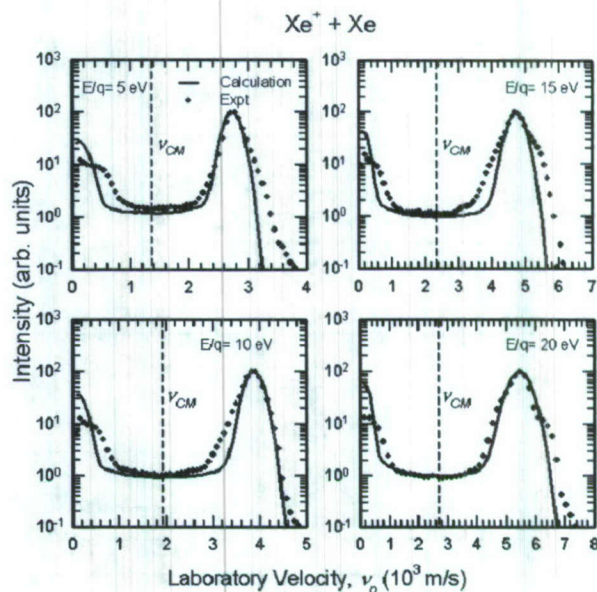(<1000 m s^{-1}) are primarily attributable to charge exchange. At the low confinement field, the overall ion transmission is reduced and no signal due to ions scattered at large angles appearing in the vicinity of the CM velocity is observed. The measurement at the high confinement field transmits ions at all scattering angles, and signal is clearly observable at all axial velocities between 0 and 2710 m s^{-1}. This is consistent with elastic scattering, for which the maximum transverse velocity corresponding to $\theta_{CM} = 90°$ is 1355 m s^{-1} at $E_T = 2.5$ eV.

Figure 4(*b*) shows an expanded view of a series of TOF velocity distributions with confinement fields corresponding to the maximum transmitted transverse velocities of 2402, 2029, 1403, 1096, 711 and 305 m s^{-1}. There is no difference between the distributions with the highest confinement fields, corresponding to the maximum transmitted transverse velocities of 2402 and 2029 m s^{-1}, indicating that full transmission of the 90° CM scattered ions occurs at both respective confinement potentials. The signal at v_{CM} is reduced by ∼1/2 at a confinement field corresponding to a maximum transmitted transverse velocity of 1403 m s^{-1}. This corresponds to a transverse kinetic energy of 1.34 eV which, within experimental uncertainties, is in good agreement with the elastic maximum transverse ion energy of 1.25 eV.

Figure 5 compares experimental and simulated axial velocity distributions for Xe$^+$ + Xe collisions at lab ion energies, E/q, of 5, 10, 15 and 20 eV. The velocity distributions are plotted on a logarithmic scale in order to expand the weak signals at larger scattering angles, corresponding to the signal in the vicinity of v_{CM}. The charge exchange and primary ion peaks of the experimental velocity distributions (symbols) appear slightly broader than the simulated bands (line). At near-thermal velocities, the shift of the experimental peak

Table 1. Morse potential parameters used for the calculation of differential scattering cross sections of the $Xe^+ + Xe$ system, where $V(R) = D_e(e^{b(r_e - R)^2} - 2e^{b(r_e - R)})$. The potentials are the averaged (u, g) pairs of potentials reported by Paidarova and Gadea [16]. All parameters are listed in atomic units.

(u, g) pair	D_e	b	r_e
Σ	0.005 85	0.645	7.476
Π	0.004 87	0.677	7.570

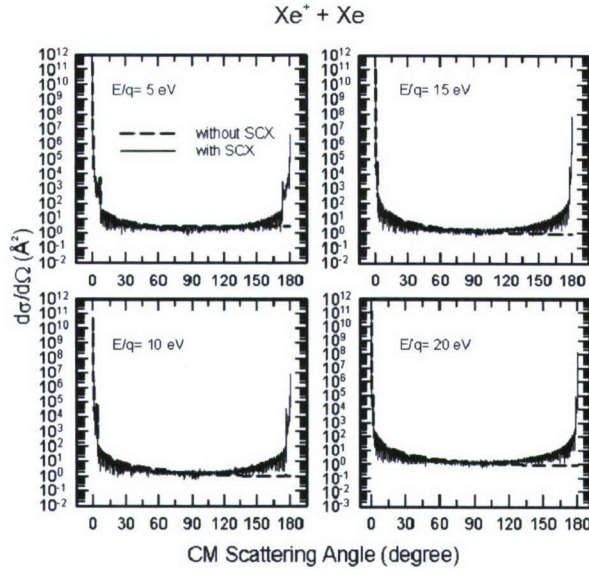**Figure 6.** Absolute elastic scattering differential cross sections for $Xe^+ + Xe$ collisions calculated using the potentials by Paidarova and Gadea [16] with (solid lines) and without (dashed lines) charge exchange.

Figure 7. Velocity inverted TOF distributions (solid circles) for $Xe^{2+}+Xe$ collisions at laboratory ion energies per charge of 5, 10, 15, 20, 30 and 40 eV. The solid lines are distributions based on elastic scattering by a combination potential (equation (7)) that provides the best agreement with experiment (parameters in table 2).

towards higher velocities can be considered an experimental artefact caused by a small potential barrier applied at the entrance of the collision cell using a cylindrical electrode surrounding the ion guide. The penetration potential barrier reflects slow, laboratory backscattered ions, thereby ensuring detection. The simulation and experimental distributions are put on the same vertical scale using the procedure described in section 3. Near v_{CM}, the simulated and experimental velocity distributions agree well within the uncertainties of the experiment, thus validating both the present approach as well as the theoretical potentials. Table 1 lists the parameters of Morse potential fits to the averaged u, g pairs of the Xe_2^+ interaction potential by Paidarova and Gadea [16].

Figure 6 plots the calculated differential cross sections as a function of CM scattering angles for lab ion energies E/q of 5, 10, 15 and 20 eV, respectively. Differential cross section calculations are shown including (solid line) and excluding (dashed line) charge exchange. The ripple in the SCX results stems from the oscillatory charge exchange probabilities.

Figure 7 compares the experimental and simulated axial velocity distributions for the $Xe^{2+} + Xe$ system at lab ion energies E/q of 5, 10, 15, 20, 30 and 40 eV. Figure 8 shows the calculated differential cross sections with and without SCX as a function of CM scattering angle. Table 2 lists the combinations
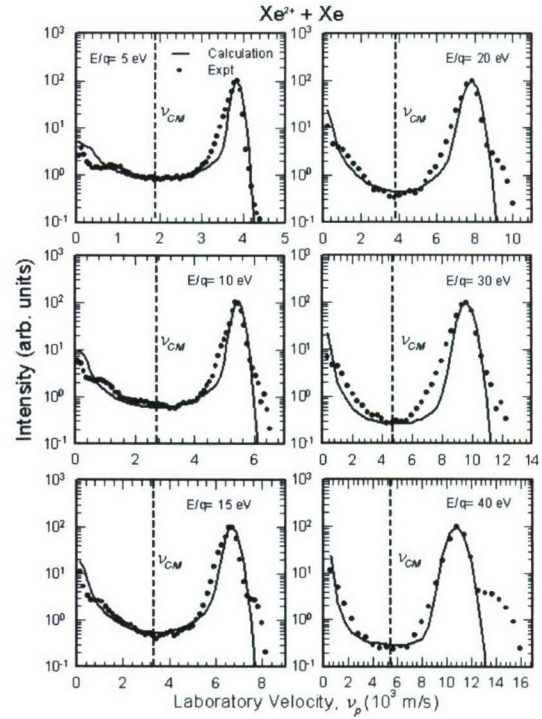
of potential parameters, a_1-a_6, that provide the best agreement between the experimental and the simulated distributions. In the vicinity of v_{CM}, the simulated distributions agree well with the experimental distributions for all collision energies. A small shoulder on the high-velocity side of the primary ion peak is seen in the experimental distributions at ion energies at and above 10 eV. Since the onset of asymmetric charge exchange leading to Coulomb channel products, $Xe^+ + Xe^+$, is around 10 eV, we attribute the shoulder to the asymmetric charge exchange channel which is expected to produce products with translational energies exceeding that of the reactants. Table 3 lists SCX integral cross sections calculated using the impact parameter model (equation (11)) for all collision energies investigated experimentally. They are consistent with previously reported experimental values [23].

4.2. Effective scattering potentials

Figure 9 plots the effective $Xe^{2+}+Xe$ interaction potential, $V^{++}(R)$, used in the simulations along with the averaged effective potential of the $Xe^+ + Xe$ interaction, $V^+(R)$, for a statistical distribution of spin–orbit states, derived from the work of Paidarova and Gadea. Also plotted in figure 9 are the Coulomb potentials associated with $Xe^+({}^2P_J) + Xe^+({}^2P_J)$, and the long-range polarization potential of $Xe^{2+} + Xe$, V_{pol}^{++}, given by
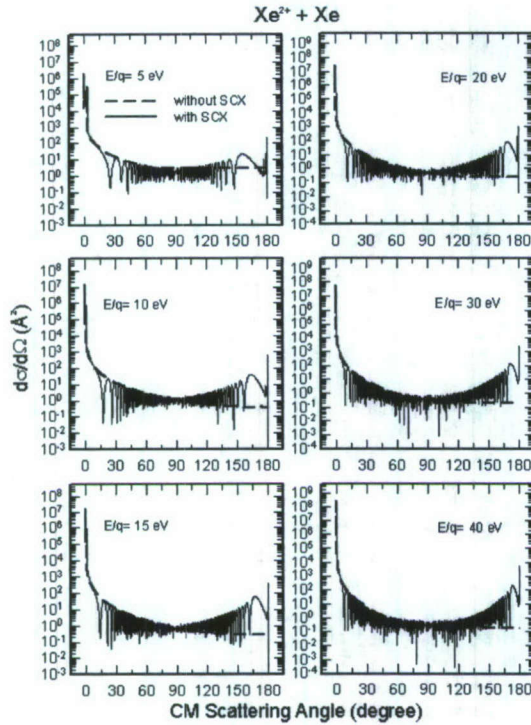
$$V_{pol}^{++}(R) = q^2\alpha_d/2R^4, \qquad (14)$$

Figure 8. Absolute elastic scattering differential cross sections for Xe^{2+} + Xe collisions calculated with the combination potential (equation (7), parameters in table 2) including (solid lines) and not including (dashed lines) charge exchange.

Table 2. Combination potential parameters (equation (7)) resulting in the best fit of the experimental differential cross section data of the Xe^{2+} + Xe collision system. a_1, a_2, a_3 are Morse potential function-like parameters, and a_4, a_5, a_6 are parameters representing a repulsive potential function form. All parameters are listed in atomic units.

a_1	a_2	a_3	a_4	a_5	a_6
0.006	0.272	11.40	1500	0	3.737

where q is the atomic charge and α_d is the dipole polarizability of Xe (4.044 Å^3) [27]. The derived potential for doubly charged ion scattering is seen to be almost parallel with the Coulomb potentials between 3 and 4 Å, above which it becomes more repulsive. The polarization and Coulomb potentials cross in the vicinity of 3 Å, which can be regarded as an interatomic distance where the electronic coupling is strong [28]. The derived potential is consistent with a potential corresponding to an adiabatic passage through the curve crossings associated with asymmetric charge-transfer transitions. In this interpretation, the potential for $R < \sim 2.5$ Å mimics the short-range Xe$^+$(^{2}P$_J$)+Xe$^+$(^{2}P$_J$) potentials, which become more repulsive than the pure Coulomb potential at short R due to the additional electron–electron repulsion. The steep repulsive part of the derived potential, $V^{++}(R)$, is also seen to be at significantly shorter distances than the effective potential, $V^+(R)$, for scattering of singly charged ions, as expected given the lower differential cross sections at large angles in the case of the Xe^{2+} + Xe system.

Table 3. SCX cross sections calculated using the impact parameter approach (equation (11)) without the inclusion of spin–orbit coupling.

E/q (eV)	σ_{SCX}(Å^2) Xe$^+$ + Xe	σ_{SCX}(Å^2) Xe^{2+} + Xe
5	81.81	26.68
10	76.75	24.85
15	73.89	23.87
20	71.89	23.14
30	66.81	22.10
40	64.98	21.40
270	54.90	17.07

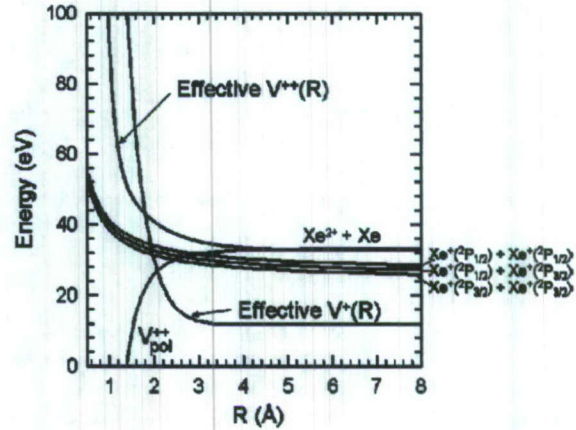**Figure 9.** Effective scattering potentials for Xe$^+$ + Xe and Xe^{2+} + Xe collisions on an energy scale given by the recombination energies of the respective ions. The Xe^{2+}+Xe long-range polarization (V_{pol}^{++}) and Coulomb potentials of the lowest spin–orbit states are also shown.

Table 4. Scattering turning points at $\theta_{CM} = 90°$ for the Xe^{2+} + Xe system and associated potential energies with respect to the Xe^{2+} + Xe asymptotic limit.

E/q (eV)	Turning point, R_0 (Å)	$V^{++}(R_0)$ (eV)
5	2.681	3.29
10	2.300	5.35
15	2.113	6.74
20	2.002	7.72
30	1.876	9.01
40	1.806	9.83
270	1.607	12.74

In order to demonstrate what region of the Xe^{2+} + Xe effective potential is relevant with respect to large-angle scattering, we list in table 4 the classical trajectory turning points associated with CM scattering angles of 90° for the investigated ion energies and an ion energy of 270 V per charge unit. The latter is the quoted peak ion energy observed for a Hall thruster operated at a typical acceleration voltage of 300 V [10]. The table demonstrates that there is only a minor displacement of the turning point between $E/q = 40$ eV, the highest experimental energy allowing reliable trapping of scattered ions, and $E/q = 270$ eV. Thus, the trajectories causing large-angle scattering at ion energies per charge between 40 and 270 eV sample a similar

J. Phys. D: Appl. Phys. **41** (2008) 165503

Y-H Chiu *et al*

region of the interaction potential. Consequently, the present derivation of the $Xe^{2+} + Xe$ effective potential should allow reasonably accurate differential cross section predictions for ions accelerated by a 300 V discharge voltage in a HET. Table 4 also lists the potential energies referenced with respect to infinitely separated $Xe^{2+} + Xe$ (asymptotic limit).

4.3. Effect of Xe^{2+} on sputtering yields

The ultimate goal of this work is to quantify sputtering currents due to elastically scattered singly and doubly charged xenon ions. Assuming a uniform axial exhaust current, the sputtering flux, F, at a particular surface off the thrust axis is given by

$$F = \int_0^\infty \frac{I_0(x)n(x)x}{r^2} \zeta(\theta_{\text{LAB}}) \, dx, \qquad (15)$$

where $I_0(x)$ is the ion current at position x with respect to the thruster exit plane, $n(x)$ is the neutral xenon atom density at x, r is the x-dependent distance to the sputtered surface and $\zeta(\theta_{\text{LAB}})$ is the differential cross section in the laboratory frame of reference:

$$\zeta(\theta_{\text{LAB}}) = \frac{d\sigma_{\text{ion}}(\theta_{\text{LAB}})}{d\Omega_{\text{LAB}}} = 4 \cos(\theta_{\text{LAB}}) \frac{d\sigma_{\text{ion}}(\theta_{\text{CM}})}{d\Omega_{\text{CM}}}. \qquad (16)$$

θ_{LAB} also depends on x; however, at significant r, the range of scattering angles associated with significant currents can be expected to be small given the rapid drop in neutral density and differential cross section with x and the associated increase in the LAB scattering angle.

The presently derived potential permits the calculation and comparison of differential cross sections for both charge states at ion energies corresponding to a typical Hall thruster discharge voltage of 300 V. It has been shown experimentally that effective acceleration voltage for ions observed in the plume of a Hall thruster is approximately 30 V below the nominal acceleration voltage [10]. We, therefore, conduct calculations for unscattered ion energies of 270 eV per unit charge. To make the differential scattering cross sections more useful to users we eliminate the SCX oscillations by applying the approximation for angles above a critical angle, $\theta_{\text{CM}} > \theta_c$:

$$\frac{d\sigma_{\text{ion}}(\theta_{\text{CM}})}{d\Omega_{\text{CM}}} = 0.5 \frac{d\sigma(\theta_{\text{CM}})}{d\Omega_{\text{CM}}} + 0.5 \frac{d\sigma(\pi - \theta_{\text{CM}})}{d\Omega_{\text{CM}}}, \qquad (17)$$

where θ_c is the angle associated with the impact parameter where $P_{\text{scx}}(b)$ becomes highly oscillatory at shorter impact parameters. The critical angles are very small at 270 eV/unit charge, approximately 1° and 3° for the singly and doubly charged systems, respectively, and equation (17) does not, therefore, affect the results at the large scattering angles of interest. The lab differential cross sections computed for $E/q = 270$ eV by this approach are shown in figure 10. From the figure it is seen that the ratio between the differential cross sections of doubly and singly charged ions at large angles is approximately 0.32.

The present cross sections permit an assessment whether elastically scattered doubly charged ions in Hall thruster plasmas contribute significantly to material erosion, and, therefore, must be considered when modelling the impact of the thruster plasma on sensitive surfaces of the spacecraft. It
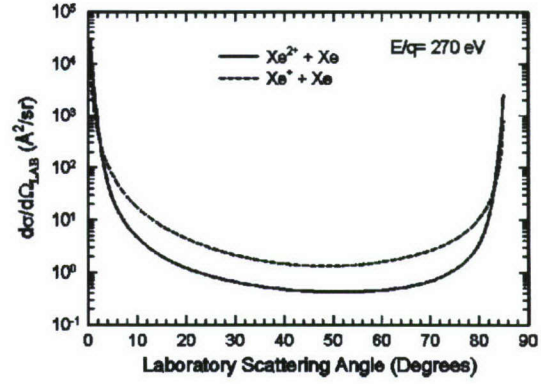

Figure 10. Laboratory differential cross sections for $Xe^+ + Xe$ and $Xe^{2+} + Xe$ elastic scattering at 270 eV ion energy per unit charge.

is safe to assume that the charge state of the sputtering ion is only relevant in terms of the kinetic energy of the incident ion, $E_{\text{LAB}}^{\text{ion}}(\theta_{\text{LAB}})$, which scales with the ion charge and depends on the elastic scattering angle (see figure 2):

$$E_{\text{LAB}}^{\text{ion}}(\theta_{\text{LAB}}) = \frac{\mu}{2} v'^2 = \frac{\mu}{2} v_{\text{LAB}}^2 \cos^2 \theta_{\text{LAB}}$$

$$= E_{\text{LAB}} \cos^2 \theta_{\text{LAB}}, \qquad (18)$$

where μ is the reduced mass of the collision system. The ratio, Ψ, between sputtering yields of doubly and singly charged ions is then given by

$$\Psi = \frac{I(Xe^{2+})Y(2E_{\text{LAB}}^+)}{2I(Xe^+)Y(E_{\text{LAB}}^+)} = \frac{(1-\alpha)\zeta^{++}v^{++}Y(2E_{\text{LAB}}^+)}{2\alpha\zeta^+v^+Y(E_{\text{LAB}}^+)}$$

$$= \frac{(1-\alpha)\zeta^{++}Y(2E_{\text{LAB}}^+)}{2^{\frac{1}{2}}\alpha\zeta^+Y(E_{\text{LAB}}^+)}, \qquad (19)$$

where $Y(E_{\text{LAB}}^+)$ is the sputtering yield at the incident ion kinetic energy for a singly charged ion, and where $E_{\text{LAB}}^{++} = 2E_{\text{LAB}}^+$. $I(Xe^{+/2+})$ are the respective ion currents, ζ^+ and ζ^{++} are the LAB differential cross sections for the singly and doubly charged ions, v^+ and $v^{++} = 2^{1/2}v^+$ are the respective ion velocities and α is the positive charge fraction attributable to singly charged ions.

A number of studies have investigated xenon ion sputtering yields for several materials [29–35]. The most commonly studied material has been molybdenum (Mo), the material for ion thruster acceleration grids. The results focus primarily on normal incidence and energies exceeding 200 eV. Doerner *et al* recently conducted the first sputtering yield measurements at energies below 200 eV [29]. There is poor agreement between the various studies, the highest energy values of Doerner *et al* being an order of magnitude lower than the lowest-energy results reported by Zalm [31], for example. Zalm successfully applied a model by Sigmund [36] to reproduce the relative energy dependence of experimental yields above 200 eV. Yamamura and Tawara published data for a large number of ions with normal incidence on elemental solids and derived an improved expression for energy dependence of absolute yields that generally resulted in values in good agreement with observations [35]. Their

Table 5. Molybdenum sputtering yields due to elastically scattered xenon ions with 270 eV per unit charge kinetic energy. E_{LAB}^+ is the laboratory or spacecraft frame energy of the ion scattered at a laboratory angle, θ_{LAB}. ζ^+ and ζ^{++} are the laboratory differential cross sections for Xe^+ and Xe^{2+} scattering, respectively. $Y(E_{LAB}^+)$ is the experimentally reported normal incidence sputtering yield. Ψ is the fraction of sputtering caused by doubly charged ions assuming a singly charged ion charge ratio, $\alpha = 0.8$.

				Doerner *et al* [29]			Yamamura and Tawara [35]		
θ_{LAB} (deg)	E_{LAB}^+ (eV)	ζ^+ (Å²/sr)	ζ^{++} (Å²/sr)	$Y(E_{LAB}^+)$ (atoms/ion)	$Y(E_{LAB}^{++})$ (atoms/ion)	Ψ	$Y(E_{LAB}^+)$ (atoms/ion)	$Y(E_{LAB}^{++})$ (atoms/ion)	Ψ
0	270.0	—	—	0.151	0.332	0.390	0.294	0.678	0.408
5	267.9	70.75	24.50	0.149	0.329	0.135	0.290	0.673	0.142
10	261.9	17.47	4.68	0.145	0.322	0.105	0.281	0.658	0.111
15	251.9	7.84	2.04	0.137	0.309	0.104	0.265	0.632	0.110
20	238.4	4.48	1.22	0.128	0.292	0.110	0.244	0.596	0.117
25	221.8	2.95	0.86	0.115	0.271	0.120	0.217	0.550	0.130
30	202.5	2.15	0.66	0.101	0.245	0.132	0.186	0.496	0.146
35	181.2	1.71	0.55	0.085	0.216	0.144	0.152	0.435	0.163
40	158.4	1.47	0.48	0.069	0.184	0.155	0.116	0.366	0.183
45	135.0	1.35	0.44	0.052	0.151	0.169	0.008	0.294	0.213
50	111.6	1.33	0.43	0.036	0.116	0.185	0.0476	0.219	0.261
55	88.8	1.40	0.43	0.021	0.083	0.210	0.0212	0.146	0.377
60	67.5	1.59	0.46	0.010	0.052	0.257	4.67×10^{-3}	0.080	0.885
65	48.2	1.95	0.53	3.46×10^{-3}	0.026	0.363			
70	31.6	2.64	0.69	4.88×10^{-4}	0.006	0.599			
75	18.1	4.24	1.13	7.46×10^{-6}	8.90×10^{-4}	5.603			

formula produces sputtering yields that are approximately a factor of 2 higher than the yields measured by Doerner *et al*.

Table 5 compares values of Ψ calculated with equation (19) and using yields obtained from a model fit to sputtering data by Doerner *et al* and the model of Yamamura and Tawara for xenon ion scattering on molybdenum assuming normal incidence and ion energy of 270 eV per unit charge and a typical singly charged ion charge fraction [10, 37], $\alpha = 0.8$. The values are listed as a function of the LAB elastic scattering angle. At $\theta_{LAB} = 0°$ corresponding to sputtering by the unscattered currents, the differential cross section is ill-defined and Ψ is calculated by setting $\zeta^+/\zeta^{++} = 1$ in equation (19). Satisfactory fits to the sputtering yield data of Doerner *et al* were obtained by applying an empirical threshold function at ion energies below 45 eV:

$$Y(E_{LAB}^{ion}) = \frac{A(E_{LAB}^{ion} - E_{th})^n}{E_{LAB}^{ion}}, \quad (20)$$

$$A = 20.25 \times 10^{-7} \quad n = 3.134 \quad E_{th} = 14.27 \text{ eV};$$

where A and n are a scaling parameter and a curvature parameter, respectively, and E_{th} signifies the sputtering threshold. At higher energies, the third order logarithmic expression provided a quality fit:

$$Y(E_{LAB}^{ion}) = -0.4567 + 0.414 \ln(E_{LAB}^{ion}) - 0.125\{\ln(E_{LAB}^{ion})\}^2$$

$$+ 0.0125\{\ln(E_{LAB}^{ion})\}^3. \quad (21)$$

Table 5 demonstrates that at scattering angles below 40°, corresponding to scattered ion energies between 158 and 270 eV per unit charge, for both sputtering yield data sets, the sputtering ratio, Ψ, between doubly and singly charged ions remains nearly constant between 0.1 and ~0.18. For sputtering due to higher scattering angles, however, the contribution due to doubly charged ions increases rapidly with angle

and declining ion energy, primarily due to the increasing ratio, $Y(2E_{LAB}^+)/Y(E_{LAB}^+)$, with decreasing incident energy per charge. This is more pronounced for the Yamamura and Tawara model that determines a significantly higher threshold of 46.8 eV. Above 60°, the Yamamura and Tawara data predict that sputtering is dominated by the doubly charged ions. Therefore, if the sputtering energy dependence reported by Doerner *et al* applies to most materials, doubly charged ions should play an important role for surfaces that are eroded due to very large-angle scattering. Note that at these large angles, most of the scattering is due to charge exchange ions.

Hall thruster insulator erosion in the discharge channel may determine the lifetime of the engine. The most commonly used insulator material is boron nitride. Sputtering yields for Xe ion beams impinging on boron nitride surfaces have been reported at ion energies above 200 eV [32, 33, 38–40]. The sputtering yields on boron nitride are found to increase by a factor of ~1.5 when the Xe ion kinetic energy is increased from 270 to 540 eV at normal incidence [32, 38]. Assuming $\alpha = 0.8$, the present large-angle differential cross sections indicate that only ~8% of observed boron nitride sputtering can be attributed to doubly charged ions. It can be assumed that in the discharge channel smaller LAB scattering angles and higher ion sputtering energies produce the highest sputtering yields, depending on the length of the channel. Garnier *et al* [39] studied the sputtering yields as a function of incident angle and found that although the sputtering yields decline with increasing angles with respect to normal incidence, the shapes of the angular dependence of the sputtering yields do not change dramatically with incident energy. At the present state of knowledge on Xe ion sputtering of boron nitride, it appears that elastically scattered doubly charged ions do not cause significant erosion in comparison with the main singly charged ions.

5. Conclusions

We present GIB–TOF measurements of absolute differential scattering cross sections, $d\sigma(v_p)/dv_p$, for the symmetric $Xe^+/Xe^{2+} + Xe$ ion–atom collision systems at several collision energies. The $Xe^+ + Xe$ differential cross sections are in good agreement with absolute differential cross sections determined using classical elastic scattering calculations based on the most recent potentials by Paidarova and Gadea. The experimental differential scattering measurements are used to derive an effective interaction potential for the $Xe^{2+} + Xe$ system. The derived potentials are used to calculate absolute differential cross sections, $d\sigma(\theta_{CM})/d\Omega_{CM}$, at an ion energy of 270 eV per unit charge, typical for plume ions of a 300 V Hall thruster. For large CM scattering angles near 90°, the differential cross sections of the doubly charged system are approximately a factor of 3 smaller than those of the $Xe^+ + Xe$ system. The differential cross sections can be applied to estimate erosion yields attributable to doubly charged ions. Using recent low-energy Xe^+–Mo sputtering data by Doerner *et al*, and a model based on compiled data by Yamamura and Tawara, and assuming 20% of positive charges are due to doubly charged ions, it is seen that the sputtering contribution by doubly charged ions does not exceed 20% for surfaces exposed to ions scattered elastically at angles below 45°. For surfaces exposed to higher scattering angles, where the incident ion energy drops below 150 eV per unit charge, the presently derived differential cross sections for doubly charged ions are needed to properly predict material erosion due to Hall thruster plasma exposure.

Acknowledgment

References

[1] Jahn R G and Choueiri E Y 2002 *Electric Propulsion* (*Encyclopedia of Physical Sciences and Technology* vol 5) (Orlando, FL: Academic)
[2] Martinez-Sanchez M and Pollard J E 1998 *J. Spacecr. Rockets* **14** 688
[3] Guerrini G, Michaut C, Bacal M, Vesselovzorov A N and Pogorelov A A 1998 *Rev. Sci. Instrum.* **69** 804
[4] Boyd I D 2001 *J. Spacecr. Rockets* **38** 381
[5] Cappaci M and Noci G 1998 *Rev. Sci. Instrum.* **69** 788
[6] Marcucci M G and Polk J E 2000 *Rev. Sci. Instrum.* **71** 1389
[7] Katz I, Jongeward G, Davis V, Mandell M, Mikellides I, Dressler R A, Boyd I, Kannenberg K, Pollard J and King D 2001 *37th AIAA/ASME/SAE/ASEE Joint Propulsion Conf. and Exhibit (Salt Lake City, UT, July)* AIAA 2001-3355
[8] Mikellides I G, Katz I, Kuharski R A and Mandell M J 2005 *J. Propul. Power* **21** 111
[9] Boyd I D and Dressler R A 2002 *J. Appl. Phys.* **92** 1764
[10] King L B and Gallimore A D 2000 *J. Propul. Power* **16** 1086
[11] Jones P R, Conklin G M, Lorents D C and Olson R E 1974 *Phys. Rev.* A **10** 102
[12] Teloy E and Gerlich D 1974 *Chem. Phys.* **4** 417
[13] Gerlich D 1992 *State-Selected and State-to-State Ion–Molecule Reaction Dynamics: I. Experiment* (*Advances in Chemical Physics* vol 82) ed C Y Ng and M Baer (New York: Wiley)
[14] Chiu Y, Fu H, Huang J and Anderson S L 1995 *J. Chem. Phys.* **115** 1228
[15] Mark S and Gerlich D 1996 *Chem. Phys.* **209** 235
[16] Paidarova I and Gadea F X 2001 *Chem. Phys.* **274** 1
[17] Dressler R A, Salter R H and Murad E 1993 *J. Chem. Phys.* **99** 1159
[18] Scott T C, Babb J F, Dalgarno A and Morgan J D 1993 *J. Chem. Phys.* **99** 2841
[19] Gerlich D 1989 *J. Chem. Phys.* **90** 127
[20] Williams S, Chiu Y, Levandier D J and Dressler R A 1998 *J. Chem. Phys.* **109** 7450
[21] Ervin K M and Armentrout P B 1985 *J. Chem. Phys.* **83** 166
[22] Child M 1974 *Molecular Collision Theory* (London: Academic)
[23] Miller J S, Pullins S H, Levandier D J, Chiu Y and Dressler R A 2002 *J. Appl. Phys.* **91** 984
[24] Pullins S H, Dressler R A, Torrents R and Gerlich D 2000 *Z. Phys. Chem.* **214** 1279
[25] Tang K T, Toennies J P and Yiu C L 1991 *J. Chem. Phys.* **94** 7266
[26] Dressler R A and Murad E 1994 Unimolecular and bimolecular ion–molecule reaction dynamics *Ion Chemistry in the Spacecraft Environment* ed C Y Ng *et al* (New York: Wiley)
[27] Radzig A A and Smirnov B M 1985 *Reference Data on Atoms, Molecules, and Ions.* (Berlin: Springer)
[28] Olson R E, Smith F T and Bauer E 1971 *Appl. Opt.* **10** 1848
[29] Doerner R P, Whyte D G and Goebel D M 2003 *J. Appl. Phys.* **93** 5816
[30] Blandino J J, Goodwin D G and Garner C E 2000 *Diamond Relat. Mater.* **9** 1992
[31] Zalm P C 1983 *J. Appl. Phys.* **54** 2660
[32] Yim J T, Falk M, Keidar M and Boyd I D 2007 *43rd AIAA/ASME/SAE/ASEE Joint Propulsion Conf. and Exhibit (Cincinatti, OH, July)* AIAA-2007-5313
[33] Yalin A P, Rubin B, Domingue S R, Glueckert Z and Williams J D 2007 *43rd AIAA/ASME/SAE/ASEE Joint Propulsion Conf. and Exhibit (Cincinatti, OH, July)* AIAA-2007-5314
[34] Williams J D, Gardner M M, Johnson M L and Wilbur P J 2003 *Report* NASA/CR-2003-212306
[35] Yamamura Y and Tawara H 1996 *At. Data Nucl. Data Tables* **62** 149
[36] Sigmund P 1969 *Phys. Rev.* **184** 383
[37] Gulczinski F S and Gallimore A D 2001 *J. Propul. Power* **17** 418
[38] Yim J T, Keidar M and Boyd I D 2006 *42th AIAA/ASME/SAE/ASEE Joint Propulsion Conf. and Exhibit (Sacramento, CA, July)* AIAA-2006-4657
[39] Garnier Y, Viel V, Roussel J F and Bernard J 1999 *J. Vac. Sci. Technol.* A **17** 3246
[40] Britton M, Waters D, Messer R, Sechkar E and Banks B 2002 *NASA Report* TM-2002-211837